

# Melt Pool Evolution in High-Power Selective Laser Melting of Nickel-Based Alloy



Borisov Evgenii, Starikov Kirill, Popovich Anatoly, and Popovich Vera

**Abstract** The paper studies melt pool evolution in nickel-based alloy as a function of the high-energy selective laser melting parameters. The influence of the geometric melt pool characteristics on the development of microstructure as well as on the formation of defects is investigated. Several laser processing parameters varying in volumetric and linear energy density were chosen. The shrinkage porosity was also studied, and its dependence on the process parameters, resulting density and microstructure were determined.

**Keywords** Single crystal alloy · Nickel-based alloy · Selective laser melting · High laser power · Additive manufacturing

## Introduction

Search for the new materials suitable for additive manufacturing (AM) of complex and high-demanding components is currently driving the future developments. There are many scientific papers devoted to the application of new materials in the additive industry [1–5]. Currently, nickel heat-resistant single-crystal alloys are the most popular in the production of blades for gas turbine engines. Direct crystallization technology of such blades is associated with the inability to fully utilize the potential of the alloy. Such a limitation is caused by the segregation of alloying elements within dendritic cells, structural heterogeneity and formation of shrinkage micropores [6]. Modern methods of additive manufacturing make it possible to control

---

B. Evgenii · S. Kirill · P. Anatoly · P. Vera (✉)  
Peter the Great St. Petersburg Polytechnic University, St. Petersburg, Russian Federation  
e-mail: [vpopovich@tudelft.nl](mailto:vpopovich@tudelft.nl)

B. Evgenii  
e-mail: [evgenii.borisov@icloud.com](mailto:evgenii.borisov@icloud.com)

P. Vera  
Faculty of Mechanical, Maritime, and Materials Engineering,  
Delft University of Technology (TU Delft), Mekelweg 2, 2628 CD Delft, The Netherlands

the microstructure of the manufactured product more precisely, which in turn can provide a higher relative density of nickel heat-resistant single-crystal alloy products [7–9]. However, the use of the selective laser melting (SLM) technique is associated with several technological problems. One of these issues is related to the specimens cracking during the growing process [10–15].

Thus, the aim of this work is to determine the dependence of the specimen's relative density and cracking on the melt pool depth formed by using various parameters of the selective laser melting process.

## Materials and Methods

The Aconity3D MIDI selective laser melting system was used for the experiment. The machine is equipped with variable focal spot diameter laser source with Gauss power distribution and a maximum power 1000 Watts. Moreover, machine is equipped with a module to enable operation with platform preheating up to 1200 °C. The parameters of the selective laser melting process were selected in such a way that different depths of the melt pools were provided during the samples production. The platform was heated to 1000 °C. This influence was realized by varying the volume and linear energy densities given to the material in the SLM process. As a result, seven scanning modes with different values of laser power, scanning speed, and hatch distance were selected. A constant layer thickness of 50 μm and laser spot diameter 400 μm was used.

The samples were made from nickel heat-resistant single-crystal alloy. The chemical composition of the powder is shown in Table 1. The powder particle size distribution was measured using Fritsch analysette 22 NanoTec plus by laser diffraction techniques.

Seven cubic samples with dimensions of 10 × 10 × 25 mm and different SLM parameters were produced. The samples were built without supports on a steel platform.

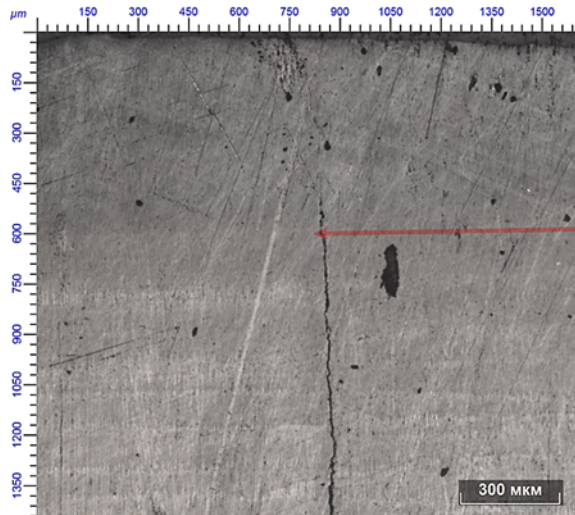
The presence of shrinkage defects was estimated based on the relative density and cross-sectional microscopy. The relative density was obtained by hydrostatic weighing (Archimedes method) of the samples.

The samples were cut along the growing direction along the line of the laser passage in the upper layer. The resulting metallographic samples were etched in a solution of HCl-20 ml, H<sub>2</sub>SO<sub>4</sub>-1 ml, and CuSO<sub>4</sub>-4 g until the visible boundaries of the melt pool appeared. The depth of the melt pool was determined graphically using the Leica DMI 5000 light optical microscope as the maximum distance (due to the

**Table 1** Chemical composition of nickel alloy powder (wt. %)

Ni	Cr	Al	Mo	W	Co	Re	Ta	Nb	C	B
60.45	4.9	5.9	1.1	8.4	9.0	4.42	4.1	1.6	0.12	0.01

**Fig. 1** Boundaries of the melt pool of sample 2. (Color figure online)



rounded shape of the boundary of the melt pool) from the upper edge of the sample to the boundary of the melt bath of the last laser pass. An example of determining the depth of a melt bath using an optical microscope is shown in Fig. 1.

Based on the data obtained, the dependence of the sample density on the depth of the melt pool provided by the scanning parameters during the production of this sample was determined.

## Results and Discussion

The powder particle size distribution measured by laser diffraction showed the following:  $D_{10} = 28.6 \mu\text{m}$ ,  $D_{50} = 55.8 \mu\text{m}$ ,  $D_{90} = 92.3 \mu\text{m}$  (Fig. 2).

Secondary electron (SE) and back-scattered electron (BSE) analysis of the powder was performed by scanning electron microscope. According to the results of the BSE analysis, it is possible to draw conclusions about the chemical uniformity of the alloy and the absence of numerous particles with surface oxide layers (Fig. 3a). Based on the results of SE analysis, it can be concluded that there are a small number of satellites and irregularly shaped particles which will not affect the fluidity of the powder during the process (Fig. 3b).

As shown in Table 2, there is no clear correlation between the values of linear energy densities and the depth of the melt pool. This can be explained by the fact that the depth of the melt pool is affected by many characteristics, and together they can give an effect that is not reflected by the linear energy density value. In addition, in this paper we used a significant heating of the working platform and the modes with large values of linear energy density. This led to the fact that the size of the melt pool in the samples is larger. Thus, it turns out that the lifetime of the melt

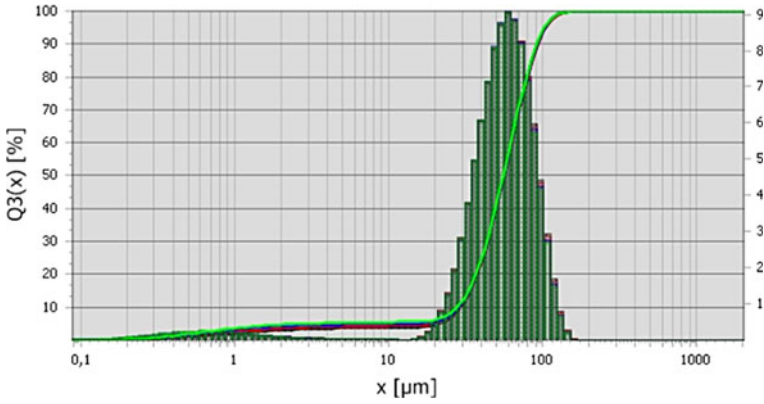


Fig. 2 Particle size distribution by volume fraction. (Color figure online)

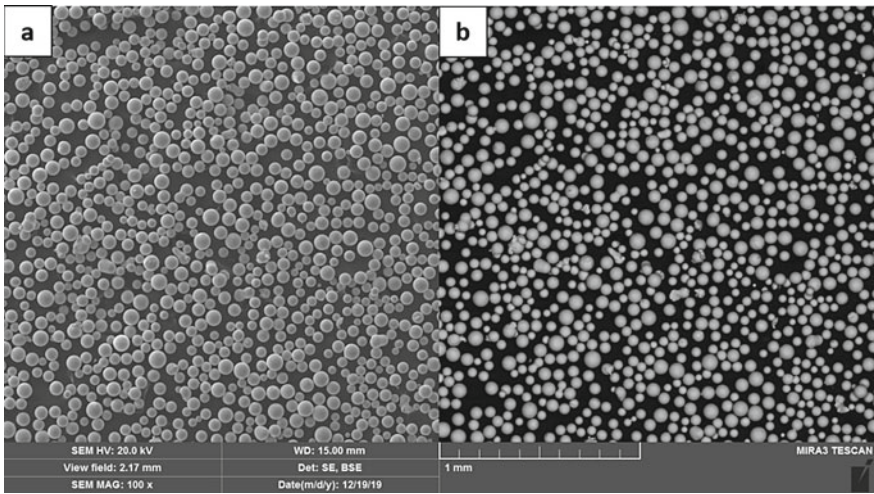


Fig. 3 Nickel heat-resistant single-crystal alloy BSE a, SE b

Table 2 Overview of the samples, showing relative density, depth of the melt pool and linear energy density

Sample №	1	2	3	4	5	6	7
Relative density, (g/mm <sup>3</sup> )	8.77	8.76	8.76	8.75	8.72	8.69	8.66
Depth of the melt pool, (µm)	690	600	510	450	360	340	320
Linear energy density, (J/mm)	0.89	0.6	0.8	0.8	0.97	0.97	0.84

pool is significantly higher than in the traditional SLM process. Apparently, these facts are the reason why there is no obvious connection between the values of the linear energy density and the depth of the melt pool. As the depth of the melt pool increases, the relative density of the samples also rises (Table 2), which indicates a decrease in the number of shrinkage defects in the samples. This effect is due to the fact that the scanning parameters that provide a greater depth of the melt pool increase the crystallization time of the upper layers of the sample which leads to a significant increase in the size of the  $\gamma$ —phase cells and a reduction in the boundary zones.

The microstructure of the obtained samples consists of elongated cells located mainly along the growing direction of the samples  $\gamma$ —solid solution with scattered particles  $\gamma'$ —phase formed on the basis of the intermetallic compound Ni<sub>3</sub>Al (Fig. 4a) which in turn consist of cuboid microparticles with an average size of  $\sim 200$  nm (Fig. 4b).

Nb and Mo carbides are isolated along the boundaries of the  $\gamma$ —phase cells. The presence of carbides of alloying elements improves the properties of heat-resistant alloys at temperatures above the solubility limit of the intermetallic  $\gamma'$ —phase (Fig. 5). However, at the same time, their presence leads to the formation of micropores of shrinkage origin.

When the melt is crystallized in boundary zones limited on the one hand by the boundaries of growing dendrites, on the other by carbides released in the melt, the melt volumes are isolated from the total volume. Then, as a result of thermal shrinkage at the crystallization front, micropores and other defects of shrinkage

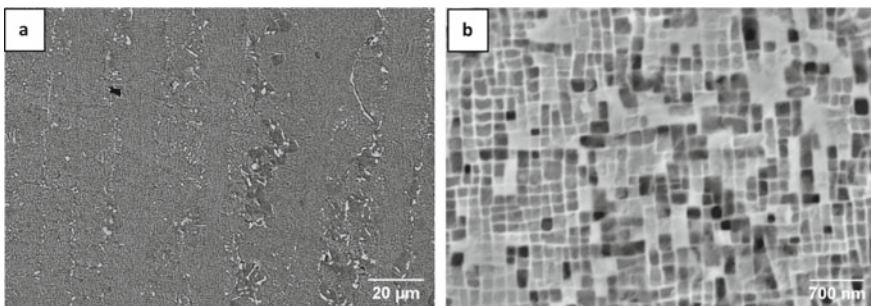


**Fig. 4** Microstructure of specimen obtained by selective laser melting

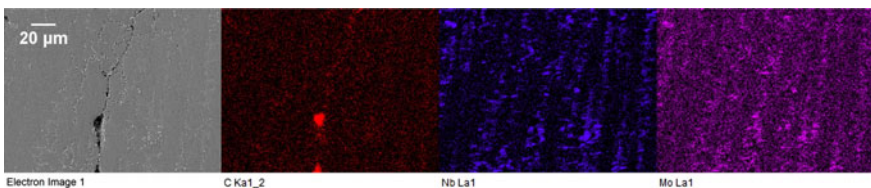


**Fig. 5** EDS of the selective laser melted specimen. (Color figure online)

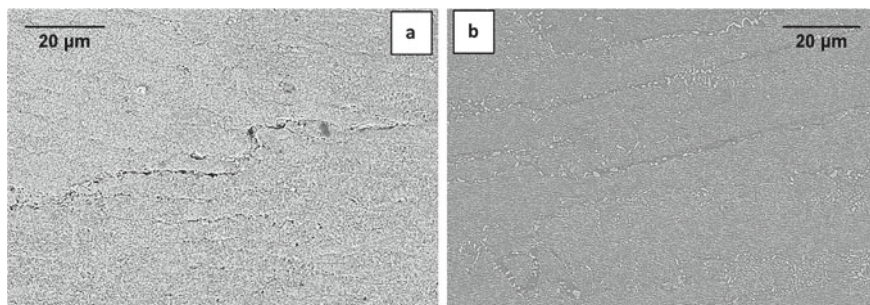


**Fig. 6** Microstructure of the specimen 7—**a** and specimen 1—**b**

origin are formed in areas isolated from the total volume of the melt due to the lack of the liquid phase. The presence of such defects in the alloy significantly reduces its performance at operating temperatures.

High crystallization rates are characterized by a smaller  $\gamma$ —PDAS (primary dendritic arm space) size and a larger overall boundary length which in turn increases the probability of shrinkage defects formation in the sample. The volume fraction of defects can be reduced by increasing the crystallization time which will ensure the growth of  $\gamma/\gamma'$ —phase cells of greater width and a reduction in the total length of the boundaries (Fig. 6).

## Conclusions

This paper presents the research results of the geometric characteristics, namely the depth of the melt pool formed during the selective laser melting of products, and its effect on the amount of shrinkage defects. The number of defects in the obtained samples was determined by the relative density, which in turn was measured by hydrostatic weighing. As a result, it was determined that as the depth of the melt pool increases, the relative density of the samples also increases. This effect is explained by a decrease in the rate of crystallization in the SLM production of samples according to the parameters that provide a greater depth of the melt pool. Slowing down the crystallization rate in the printing process provides a greater growth of  $\gamma$ —phase cells and, as a result, a decrease in the volume fraction of  $\gamma'$ —phase in which the formation of shrinkage defects occurs.

**Funding** This research was supported by Russian Science Foundation grant (project No 19-79-30002).

## References

1. Chauvet E, Tassin C, Blandin JJ, Dendievel R, Martin G (2018) Producing Ni-base superalloys single crystal by selective electron beam melting. *Scripta Mater* 152:15–19
2. Polozov I, Sufiiarov V, Popovich A, Masaylo D, Grigoriev A (2018) Synthesis of Ti-5Al, Ti-6Al-7Nb, and Ti-22Al-25Nb alloys from elemental powders using powder-bed fusion additive manufacturing. *J Alloy Compound* 763:436–445
3. Goncharov IS, Razumov NG, Silin AO, Ozerskoi NE, Shamshurin AI, Kim A, Popovich AA et al (2019) Synthesis of Nb-based powder alloy by mechanical alloying and plasma spheroidization processes for additive manufacturing. *Mater Lett* 245:188–191
4. Razumov NG, Popovich AA, Grigor'ev AV, Silin AO, Goncharov IS (2019) Morphology of high-strength heat-resistant steel powder for machines for additive production from shavings. *Met Sci Heat Treat* 60(11–12):710–714
5. Xu J, Lin X, Guo P, Dong H, Wen X, Li Q, Huang W et al (2018) The initiation and propagation mechanism of the overlapping zone cracking during laser solid forming of IN-738LC superalloy. *J Alloy Compd* 749:859–870
6. Zavodov AV, Petrushin NV, Zaitsev DV (2017) Microstructure and phase composition of ZHS32 superalloy after selective laser melting, vacuum heat treatment and hot isostatic pressing. *Lett. Mater.* 7(2):111–116
7. Popovich VA, Borisov EV, Sufiyarov VS et al (2019) Tailoring the properties in functionally graded alloy inconel 718 using additive technologies. *Met Sci Heat Treat* 60:701–709
8. Sufiiarov VS, Popovich AA, Borisov EV, Polozov I (2015) Selective laser melting of titanium alloy and manufacturing of gas-turbine engine part blanks. *Tsvetnye Metally* 8:76–80
9. Sh Sufiyarov V, Borisov EV, Polozov IA, Masaylo DV (2018) Control of structure formation in selective laser melting process. *Tsvetnye Metally* 7:68–74
10. Kou S (2015) A criterion for cracking during solidification. *Acta Mater* 88:366–374
11. Qiu C, Chen H, Liu Q, Yue S, Wang H (2019) On the solidification behaviour and cracking origin of a nickel-based superalloy during selective laser melting. *Mater Charact* 148:330–344
12. Yang J, Li F, Wang Z, Zeng X (2015) Cracking behavior and control of Rene 104 superalloy produced by direct laser fabrication. *J Mater Process Technol* 225:229–239
13. Han Q, Mertens R, Montero-Sistiaga ML, Yang S, Setchi R, Vanmeensel K, Fan H et al (2018) Laser powder bed fusion of Hastelloy X: effects of hot isostatic pressing and the hot cracking mechanism. *Mater Sci Engi: A* 732:228–239
14. Liu Z, Qi H, Jiang L (2016) Control of crystal orientation and continuous growth through inclination of coaxial nozzle in laser powder deposition of single-crystal superalloy. *J Mater Process Technol* 230:177–186
15. Borisov EV et al (2020) Selective laser melting of Inconel 718 under high laser power. *Mater Today: Proc*